

Structural Design and Aeromechanical Analysis of Unconventional Blades for Future Mars Rotorcraft

Ravi Lumba*
Graduate Research Assistant

Cheng Chi
Graduate Research Assistant
University of Maryland, College Park, MD

Anubhav Datta
Associate Professor

Witold Koning

Natalia Perez Perez
Aerospace Engineer
NASA Ames Research Center, Moffett Field, CA

Haley Cummings

The structural design of rotor blades with ultra-thin, unconventional airfoils is conducted in support of the NASA Rotor Optimization for the Advancement of Mars eXploration (ROAMX) project. The outer mold line was provided by NASA, and the internal structural design was developed at the University of Maryland using a CAD-based three-dimensional (3D) aeromechanical analysis. The main objectives of this paper are to document the unique aeroelastic behavior encountered due to the low Reynolds number (down to 15K) and high subsonic Mach number (up to 0.95). Four different blade designs are considered, with the pitch axis varied from quarter-chord to midchord to determine the effect of center of gravity (C.G.) offset on natural frequencies, blade deformations, root loads, and 3D stresses. Torsional stability is emphasized for each of the designs - especially important due to the low Lock number on Mars. The designs are first studied in vacuum, and significant reductions in root loads and 3D stresses are achieved by moving the pitch axis closer to midchord to reduce the C.G. offset. Next, the design with the pitch axis at 40% chord is selected for a lifting-line aeromechanical analysis. The blade control load, airloads, deformations, and 3D stresses are studied for steady hover. Dynamic control load and dynamic 3D stresses are studied for unsteady hover. Interesting elastic twist is observed due to the trapeze effect and propeller moment, in turn affecting the spanwise distribution of aerodynamic loads. The dynamic control load is found to increase significantly due to inertial coupling from the C.G. offset. The dynamic stresses also increase but still have factors of safety greater than two for both tensile and compressive stress.

Nomenclature

A	disk area, m ²
A_b	projected blade area, m ²
C_T	thrust coefficient, $T/\rho AV_i^2$
C_T/σ	blade loading, $T/\rho A_b V_i^2$
C_P	power coefficient
c	chord, m
E_1	longitudinal Young's modulus, GPa
E_2	transverse Young's modulus, GPa
F_Y	root lag force, N
G	shear modulus, GPa
M	Mach number
M_X	root torsional moment, N-m
M_Y	root flapping moment, N-m
R	rotor radius, m
Re	Reynolds number
t	blade thickness, m
V_t	tip speed, ωR
θ_{75}	collective pitch at 75% radius, deg
θ_{1c}	lateral cyclic, deg
ν_{12}	Poisson's ratio
σ	rotor solidity, $A_b/\pi R^2$
σ_{11}	axial stress, Pa
σ_{22}	in-plane stress, Pa
ω	rotational speed, rad/s

Introduction

On April 19, 2021, the Mars Helicopter (MH) Ingenuity demonstrated the first powered flight on another planet, opening a new era in aeronautics and Mars exploration. The dream of rotorcraft flight on Mars (Refs. 1–3) was realized.

The 1.8-kg MH is a technology demonstrator with no payload, designed to inform our understanding of basic Martian aeronautics (Refs. 4,5). Science missions will require larger platforms with longer endurance and greater payload. NASA and Jet Propulsion Laboratory have proposed follow-on conceptual designs, with the University of Maryland conducting preliminary structural design of the rotor blades (Ref. 6). Two configurations were proposed—a coaxial and a hexacopter. They cover seven designs as presented in Table 1, with the MH listed for comparison. Two designs use coaxial rotors: a 4.6-kg Advanced Mars Helicopter (AMH) with the same rotor radius as MH and a 19.3-kg Mars Science Helicopter (MSH) with a rotor radius of 1.25 m. The other five designs are the hexacopters with a rotor radius of 0.64 m, each optimized for a different payload, range, and landing site.

The structural design and aeromechanical analysis of the MSH Hexa baseline, shown in Fig. 1, was reported in Ref. 7. Sharp-edged, ultra-thin airfoils designed in Ref. 8 for low Reynolds number (Re) were used. Significant twist deformations were observed, driven by the low torsional stiffness of the thin blades. Unlike conventional rotors, the elastic twist was not due solely to the propeller or aerodynamic moment but also the trapeze effect, which must be considered for ultra-thin blades. An important observation was that the movement of the pitch axis was useful to reduce the loads without much adverse effect on stability. Both conclusions illustrated the unconventional behavior of these unique blades and the need for further studies.

*Corresponding author; email:rlumba@umd.edu.

Final version of paper presented at the VFS Transformative Vertical Flight 2022, San Jose, CA, January 25–27, 2022. Manuscript received July 2022; accepted February 2023.

Table 1. Next-generation NASA Mars helicopter designs; MSH Hexacopters named after landing sites

Aircraft	Radius (m)	Mass (kg)	Payload (kg)
MH	0.605	1.8	0
AMH	0.605	4.6	1.3
MSH Coax	1.25	19.3	2.02
MSH Hexa Baseline	0.64	17.7	2.02
MSH Hexa Max cap ^a	0.64	31.2	0, 2, 5, 8
MSH Hexa Milankovic	0.64	17.12	2.1
MSH Hexa Becquerel	0.64	20.73	2.7
MSH Hexa Palikir	0.64	21.03	2.1

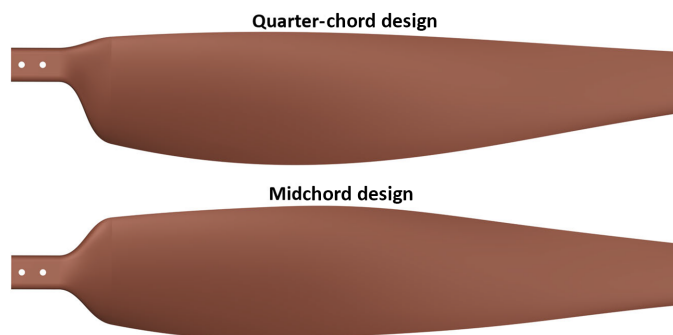
^aMaximum capacity of various ranges.

To support the next generation of Mars rotorcraft, NASA recently launched the Rotor Optimization for the Advancement of Mars eXploration (ROAMX) project (Ref. 9) to fabricate and test a set of future rotor blades. These blades are not specific to any particular configuration but meant to reproduce the unconventional aerodynamic and structural behavior expected on Mars in a generic manner. Independence from configuration meant no hard constraint on flap frequency for aircraft control. But testing on Earth meant testing at high speeds of sound, which for Mars-like tip Mach numbers meant high rotational speed, hence greater centrifugal forces. Hence the design goals were different from those in Ref. 7. These blades are the subject of this paper. Overall, the ROAMX project seeks to develop an optimized Mars rotor using unconventional airfoils and rotor blades to significantly increase payload capacity, speed, and range for next-generation Mars rotorcraft. The approach consists of a computational and experimental investigation of Martian aerodynamics and dynamics.

The University of Maryland is one of the collaborators on the ROAMX project. Previous research (Refs. 8, 10–12) has shown that utilizing thin, unconventional airfoils can bring aerodynamic benefits on Mars. As part of this effort, the University of Maryland is researching the structural dynamics and aeroelastic behavior of such blades. The primary focus of this paper was on the structural design and aeroelastic analysis of a representative blade. The analysis used a full 3D CAD-based description of the structure. Stability, airloads, deformations, control loads, and 3D stresses were predicted. The placement of the pitch axis was varied to study the effect on root loads, 3D stresses, and stability, similar to what was done in Ref. 7.

Technical Approach

The structural design of the blade is discussed before the detailed analysis begins. To observe the effect on aeroelastic behavior, four different blade designs were developed, each with the pitch axis at a different location between quarter-chord and half-chord. Next, the blade stability was calculated for each of the four rotor models to determine the effect of pitch axis placement on stability. Then, a detailed 3D finite element analysis (FEA) was carried out to investigate the natural frequencies, root loads, blade deformation, and 3D stresses due to rotation in vacuum. Based on the stability and 3D stresses, a single blade design was chosen for aeromechanical analysis. The blade was first studied in ideal hover, and the airloads, deformations, control load, and 3D stresses are presented. Finally, lateral cyclic was added in hover, and the dynamic stresses and control load were studied to investigate the response of the blade to small perturbations present in experimental hover testing. The airfoil decks needed in the analysis were provided by NASA. Throughout the paper, particular attention was paid to the influence of the trapeze effect and the effect of moving the pitch axis back from the conventional location at the quarter-chord toward midchord.

**Fig. 1. MSH hexacopter proposed by NASA (Ref. 6).****Fig. 2. Blade CAD models with pitch axis at quarter-chord and midchord.**

Tools

The CAD designs were constructed in CATIA, and the flexible parts of the design were meshed in Cubit with higher order hexahedral elements. The connection between flexible parts and connections to the rest of the hub were modeled as multibody joints. The analysis was performed using the U.S. Army/University of Maryland code X3D (Refs. 13–16). X3D uses lifting line aerodynamics—with C81 airfoil decks and free wake—and has a built-in 1D-to-3D aerodynamic-to-structures interface. The interface was verified under Martian conditions by the authors in Ref. 12 for an ultra-thin rotor tested in hover in a vacuum chamber.

Structural Design

The rotor used in this study was a four-bladed hingeless rotor with a radius of 0.72 m and a geometric solidity of $\sigma = 0.12$. The design requirement was for the blade to withstand tip Mach numbers ranging from 0.7 up to 0.95 for Earth air composition at reduced pressures (18 mbar). Due to the higher speed of sound on Earth, the rotational speed must be higher than on Mars to match the Mach number, resulting in high inertial loads that must be withstood by the ultra-thin blade. In addition to the blade, a significant portion of this work involved designing a blade adapter to connect the blade to the hub structure. The blade adapter is included in the coupled analysis, and, similar to the blade, has its structural design verified using the 3D stresses. However, due to their proprietary nature, both the blade adapter and the hub structure cannot be shown in the paper.

Four different blade designs were developed and analyzed. The first one was a baseline design with the pitch axis located at the quarter-chord. Due to the low Lock number, leading-edge weights are not needed for stability. However, the resultant large chordwise center of gravity (C.G.) offset generates high root loads that may increase the weight of the hub and control system. Therefore, three other designs—with the pitch axis located at 35%, 40%, and 50% chord—were considered to reduce the C.G. offset. Figure 2 shows the geometry for the two extreme designs—pitch axis at quarter-chord and midchord.

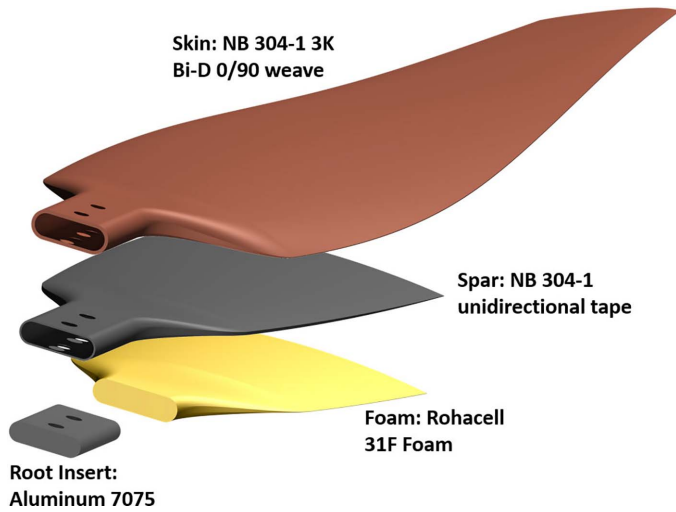


Fig. 3. Materials and internal structure of the blade design.

Table 2. Airfoil thickness breakdown

r/R (%)	Total Thickness (t/c)	Foam Thickness (% t)	Spar Thickness (% t)	Skin Thickness (% t)
25	6	48.0	22.5	29.5
35	2.9	45.1	27.7	27.2
45	1.4	0	46.3	53.7
50	1	0	0	100

A highly cambered airfoil with a thickness-to-chord ratio (t/c) of 6% is used at 25% R . This transitions to an ultra-thin airfoil by 50% R , with a t/c of 1% similar to those introduced in Ref. 8. Outboard of 50% R , the thickness remains 1% chord, although the airfoil changes along the span.

Figure 3 shows the internal blade structure. The structural design was created to minimize weight while ensuring a sufficient factor of safety. An important consideration was manufacturability. The root insert is made of 7075 aluminum, starting at $r/R = 12%$ and ending at $r/R = 18%$. From 18% to 35% radius there is a foam core made of Rohacell 31F foam. Surrounding the root insert and foam is the spar, which consists of a unidirectional tape made with NB 304-1 resin with standard modulus carbon fiber. The fibers are parallel to the blade radial direction for the full spar. The spar starts at the root insert with three plies and has a one ply drop-off between $r/R = 25%$ and $r/R = 35%$. From 35% to 45% radius, there is no foam core, so the spar fills the cross section not occupied by the skin. The skin is wrapped around all components and consists of a carbon fiber weave made up of NB 304-1 resin and 3K plane Bi-D

Table 4. ROAMX blade mass breakdown

Component	Mass (g)	Mass Fraction (%)	C.G Location	
			In-plane	Out-of-Plane
Root insert	24	14.3	0	0
Foam	0.68	0.4	8.7	3.4
Spar	37.7	22.4	5.3	2.6
Skin	105.6	62.9	-0.9	-0.4

0/90 weave. The weave is oriented so that one set of fibers is parallel to the blade radial direction, while the other is parallel to the chordwise direction. There are six layers of skin at the root insert, with a two ply drop-off in the transition region to 25% radius and an additional two ply drop-off until 35% radius. The skin remains two plies until the spar ends at 45% radius, after which the blade is entirely made of skin.

Table 2 presents the thickness breakdown for each inboard cross section, including the airfoil t/c and the relative thicknesses of each component. These values are obtained at the point of maximum thickness. Outboard of 50% radius, the blade is completely composed of skin.

Material modeling

Table 3 presents the ROAMX material properties. Aluminum and foam are isotropic materials, so $E_1 = E_2$, and $G = E/2(1 + \nu_{12})$. The composite materials are modeled as transversely isotropic, with the properties in the thickness direction assumed equal to the transverse direction. The composite material properties were obtained from the manufacturer. The measured properties of composites used at the University of Maryland are shown for comparison. One interesting observation is that the E_1 of the skin is close to that of the spar. This, coupled with the higher curvature found in the skin, will cause the skin to carry the highest stresses.

The material properties in Table 3 are provided in the material axis system. However, X3D requires them in the global blade frame, which means that the nonisotropic (composite) materials must be converted using the blade twist and the ply orientation. The stresses calculated by X3D are in the blade frame, so a similar method is used to convert the stresses back to the material axis for the factor of safety calculation using the allowable strength.

Inertial properties

The total blade mass is 168 g, with Table 4 presenting a breakdown of each component, including the mass and the C.G. location in both the in-plane (chordwise) and out-of-plane (thickness-wise) directions. The mass breakdowns are the same for the four designs, but the C.G. is given for the blade with the pitch axis at 50% chord with respect to the chord at

Table 3. ROAMX material properties

Property	Aluminum	Rohacell 31F	Weave		Uni Tape	
			ROAMX	UMD	ROAMX	UMD
Density (kg/m ³)	2810	35	1480	1470	1550	1775
E_1 (GPa)	71.7	0.036	89.6	81.5	114.45	133.1
E_2 (GPa)	71.7	0.036	89.6	72.9	9.89	10.3
G_{12} (GPa)	26.9	0.013	4.14	5.54	4.14	6.35
ν_{12}	0.33	0.38	0.05	0.08	0.29	0.34
Tensile strength (MPa)	503	1.0	586	-	1992	2723
Compressive strength (MPa)	503	0.4	467	-	951	1689

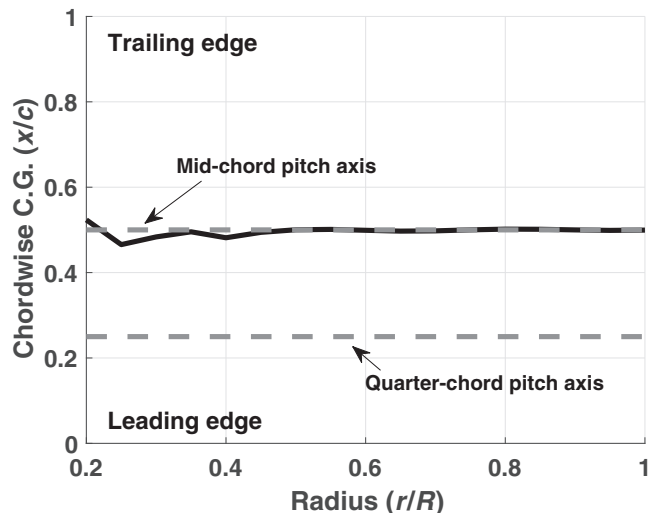


Fig. 4. Chord-wise C.G. location.

75% radius. The collective is set to be zero at 75% radius. The physical C.G. location will remain relatively constant for each of the designs but varies due to the offset in the pitch axis. A positive offset signifies the C.G. is ahead of the pitch axis or above the plane of rotation, while a negative value means the C.G. is behind the pitch axis or below the plane of rotation. The overall C.G. is approximately 0.7% chord ahead of midchord and 0.3% chord above the plane of rotation.

The chordwise C.G. is presented versus radius in Fig. 4 for the design with the pitch axis at 50% chord. For each of the four designs, the C.G. varies in the transition region (up to 25% radius) but is identical outboard of this. Even though the airfoils are not symmetric, the C.G. is located close to the midchord because the skin and spar account for over 99% of the weight (not including the aluminum root insert) and are equally distributed around the outside of the airfoil. This leads to a large C.G. offset for the quarter-chord design. The C.G. offset from the pitch axis was changed through movement of the pitch axis, as the blade C.G. outboard of the transition region remained constant. As seen in Fig. 4, the C.G. offset is nearly eliminated by moving the pitch axis to midchord.

3D structural model

The blade and blade adapter were meshed separately but connected through multibody joints and analyzed as a coupled system. The meshes for the quarter-chord and midchord blade designs are presented in Fig. 5. All four blade designs had 20,147 nodes and 2202 higher-order 27-noded hexahedral brick elements. For the blade mesh, one element was used through the thickness for the skin, spar, and foam, for a total of five elements in the thickness direction. This followed the approach used by Chi (Ref. 16) and Sutherland (Ref. 17) for advanced geometry composite rotors, which showed good agreement between X3D and experimental strain measurements. The mesh was refined in the root section for two reasons: (1) the geometry is complicated, so a finer mesh is needed for good-quality elements, and (2) the root is where the highest stresses were observed during preliminary designs. The blade adapter had 6766 nodes and 606 higher-order 27-noded hexahedral brick elements, bringing the total number of degrees of freedom for the system to approximately 75K.

There were five multibody joints used in the analysis to model the connections between physical parts and simulate the load path. Figure 6 shows the connections from the blade through the blade adapter to the hub. There are two bolts that connect the blade and blade adapter. Each

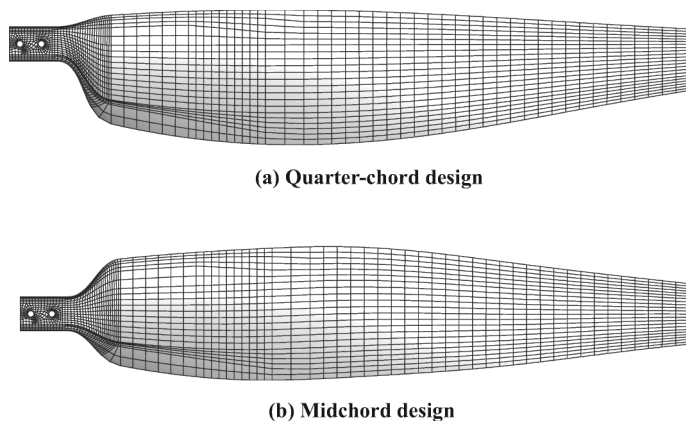


Fig. 5. Blade meshes for two extreme designs.

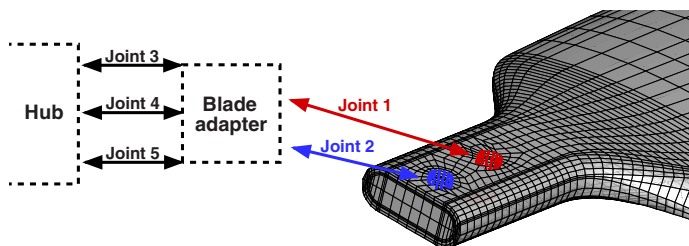


Fig. 6. There are five multibody joints that connect the blade, blade adapter, and hub.

bolt was modeled as a separate joint with all degrees of freedom locked, meaning that the two bodies (blade and blade adapter) could have no relative motion at these points. All of the loads from the blade were transferred into the blade adapter through the two joints. The three joints that connect the blade adapter to the hub were individually constructed to match the physical load path through joints stiffness and degrees of freedom.

Blade Stability

This section studies the torsional stability of the four blade designs. An extremely low torsional stiffness, combined with a low Lock number and large C.G. offset mean that the blade stability must be carefully evaluated, focusing on the torsional stability. In addition to the low damping due to the Lock number, moving the pitch axis back toward midchord will cause an additional decrease in torsional damping. Although previous studies indicate that this will reduce loads, a balance between stability and loads must be found.

The torsional stability of the blade is calculated using the following procedure. First, the rotor solution was converged for a high collective of 20°. Next, a 3° step input was applied, and the transient response was measured. The blade stability is obtained for the highest tip Mach number of 0.95. The damping is extracted from the transient response using Prony’s method. To measure the algorithmic damping inherently present in X3D, the same procedure was followed, but the aerodynamics were turned off by setting density to zero right after the step input. The algorithmic damping is subtracted from the cases with aerodynamics to determine the true aerodynamic damping. The algorithmic damping varies for each mode but is typically between 2% and 3% .

Figure 7 presents the transient response at the tip for the quarter-chord and midchord designs. There are three things to note in Fig. 7. First, even

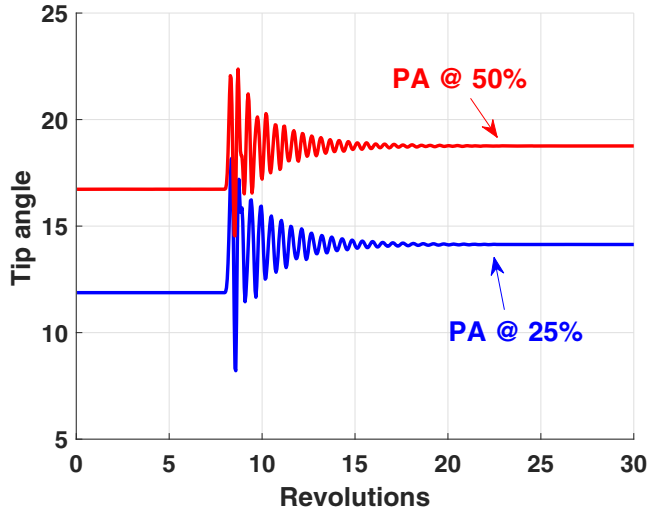


Fig. 7. The tip pitch angle transient response is shown for the quarter-chord and midchord designs.

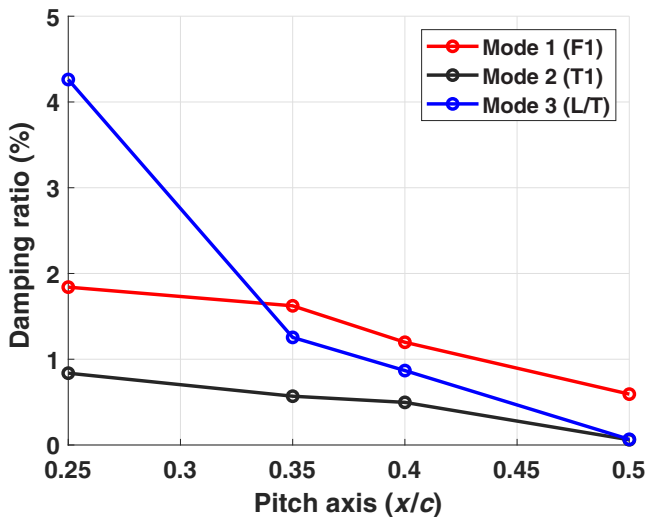


Fig. 8. Damping versus pitch axis location.

though the blades have the same root collective, the tip angle varies by over 4°. Second, even though the collective step was 3°, the tip angle only changes by just under 2.5°. Both of these are due to large twist deformations that will be explored in the next section. Lastly, it is seen that the solution does damp out, but requires nearly 15 revolutions, an artifact of the ultra-low Lock number.

Figure 8 shows the damping for the first three modes versus pitch axis location. The first mode is the first flap, the second mode is the first torsion, and the third mode is a coupled lag/torsion mode. The damping ratios are low for all designs and modes but follow a clear trend of decreasing as the pitch axis moves back to midchord. As expected, the torsional damping is the lowest, with all damping ratios under 1%. The effect of pitch axis location is extremely significant for the coupled lag-torsion mode damping, dropping by almost two orders of magnitude when the pitch axis is moved from quarter-chord to midchord. If a blade design was to be chosen solely based on the damping ratio, the baseline quarter-chord model would be selected. However, the 3D stress will be considered along with blade stability when choosing a design for detailed aeromechanical analysis.

Rotation in Vacuum

This section studies the structural response in vacuum. The root loads, blade deformations, 3D stresses, and natural frequencies are presented. The blade is analyzed at a variety of tip Mach numbers ranging from nonrotating to 0.95; however, only results from the highest case are shown here as these produce the largest loads and deformations. Although these results were obtained in vacuum, the rotational speed is described in terms of the equivalent tip Mach number in the presence of air. At the end of this section, one blade design will be chosen for aerodynamic analysis based on the stresses and stability. Studying the behavior of the ultra-thin blades in vacuum is important, as it allows for the inertial coupling caused by the unique blade design and pitch axis location to be isolated without the complications of aerodynamics.

Blade root loads

In this section, the blade root loads are studied for different pitch axis locations and collectives to observe the effect of in-plane and out-of-plane C.G. offset. The lead-lag force, blade torsional moment, and blade flapping moment were studied, as these loads are the most affected by the relocation of the pitch axis (changing the C.G. offset). The sign

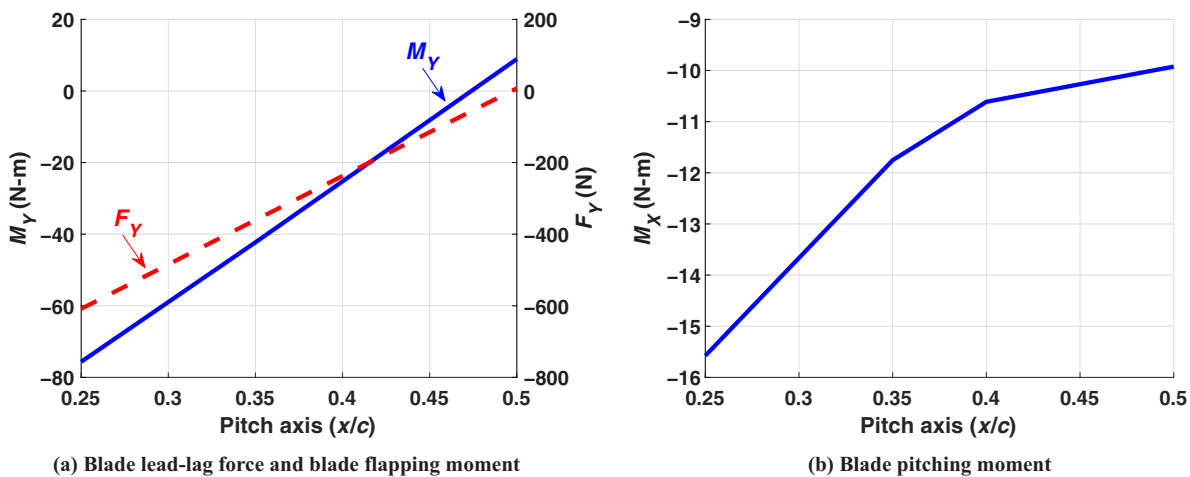


Fig. 9. Blade root forces versus pitch axis for a collective of 20°.

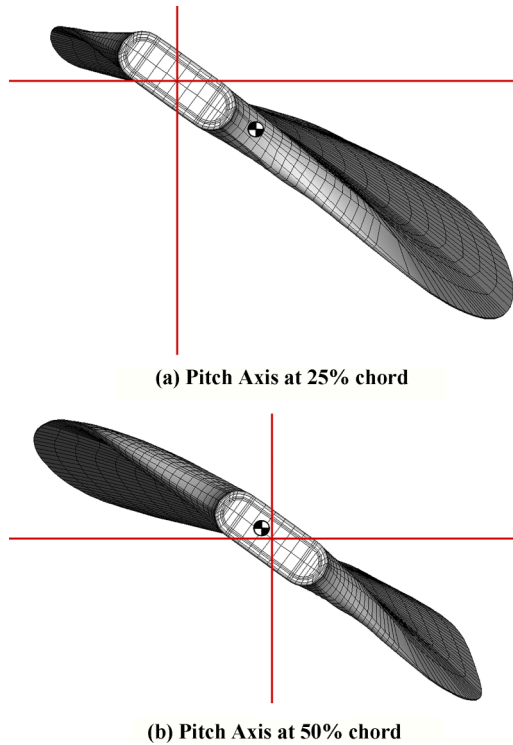


Fig. 10. Center of gravity location for two blade designs at a collective of 20°.

convention for the root loads is as follows: the lead-lag force (F_Y) is positive toward the leading edge, the torsional moment (M_X) is positive nose-up, and the bending moment (M_Y) is positive flap down.

The lead-lag force and blade flapping moment are presented in Fig. 9(a) for varying pitch axis locations and a collective of 20°. Figure 10 presents a cross-sectional view of the blade root with the C.G. marked for the two extreme cases—pitch axis at quarter-chord and midchord. As was seen in the previous section, the blade C.G. remains close to the midchord along the entire radius (Fig. 4); therefore, when the pitch axis was located at 25% chord the in-plane component of the centrifugal force caused a large lag force. The large C.G. offset had a similar effect on the blade flapping moment. For a high pitching angle

and the pitch axis at quarter-chord, the blade C.G. dropped below the plane of rotation, causing a large flap up moment.

When the pitch axis is moved toward midchord, the in-plane C.G. offset drastically reduces by about two orders of magnitude, causing the lag force to decrease by a similar amount. The C.G. is now located in front of the pitch axis, causing a change in the lag force direction. A similar trend is observed for the blade flapping moment. When the pitch axis is moved from quarter-chord to midchord, the C.G. offset reduces by an order of magnitude and moves from below to above the plane of rotation, causing the moment to decrease by an order of magnitude and switch from flap up to flap down. Both the lag force and blade flapping moment could be drastically reduced by moving the pitch axis to midchord, reducing the in-plane and out-of-plane C.G. offsets.

Figure 9(b) shows the blade torsional moment versus pitch axis for the same conditions as above. Similar to the lead-lag force and flapping moment, the C.G. offset caused a high torsional moment when the pitch axis was located at quarter-chord, this time through the propeller moment. The propeller moment is a torsional moment due to the in-plane component of centrifugal force that acts on any rotor with a nonzero collective. The propeller moment will attempt to flatten the blade and acts opposite to the local pitch angle (positive pitch causes nose-down moment and vice versa). However, unlike for the lead-lag force and blade flapping moment, eliminating the C.G. offset did not bring the net load close to zero. The high twist and rotational speed mean that a high propeller moment was still present, even with the pitch axis at midchord.

Figures 11(a) and 11(b) show the same loads, but now the variation with collective is studied. Only the two extreme blade designs (pitch axis at 25% chord and pitch axis at 50% chord) are shown. It is clear that the lag force remained relatively constant with collective, as the lateral change in C.G. with moderate collective was negligible. However, the blade flapping moment did vary with collective, but only when the pitch axis was at quarter-chord. This is because the blade flapping moment is dependent on the out-of-plane C.G. offset, which varies drastically with collective when the pitch axis was at quarter-chord. However, the total C.G. offset was almost zero for the pitch axis at midchord, and therefore the out-of-plane C.G. offset remains small with collective.

For both designs, the blade torsional moment (Fig. 11(b)) decreased with collective due to the reduction in propeller moment. Overall, it was seen that moving the pitch axis toward midchord could significantly reduce the blade torsional moment by up to 35% and almost eliminate the in-plane root shear and blade flapping moment. The reduction in

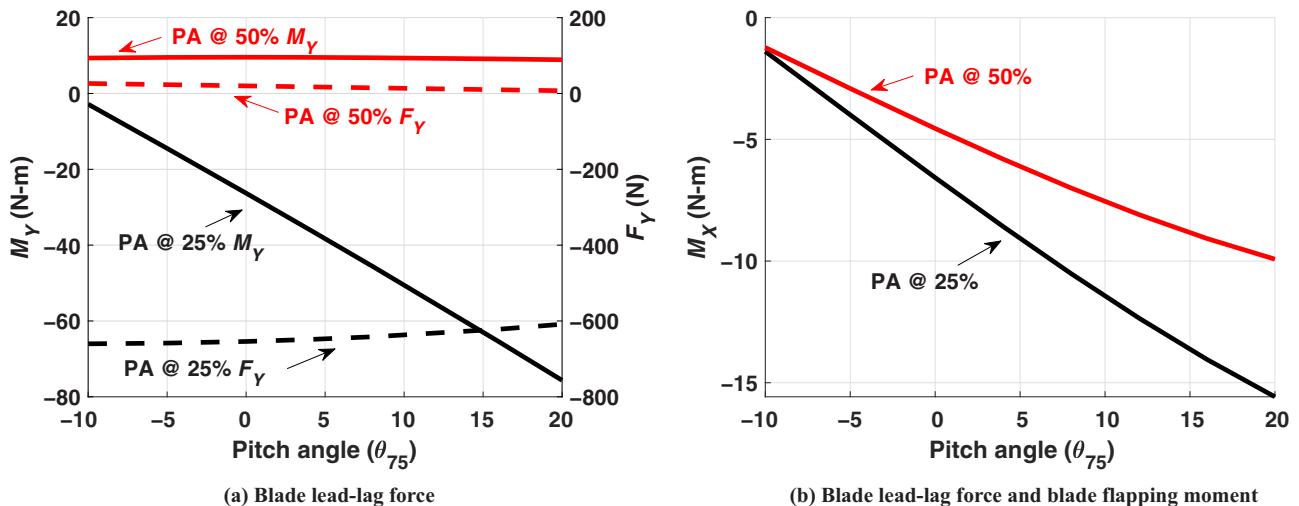


Fig. 11. Blade root forces versus θ_{75} for pitch axis at quarter-chord and midchord.

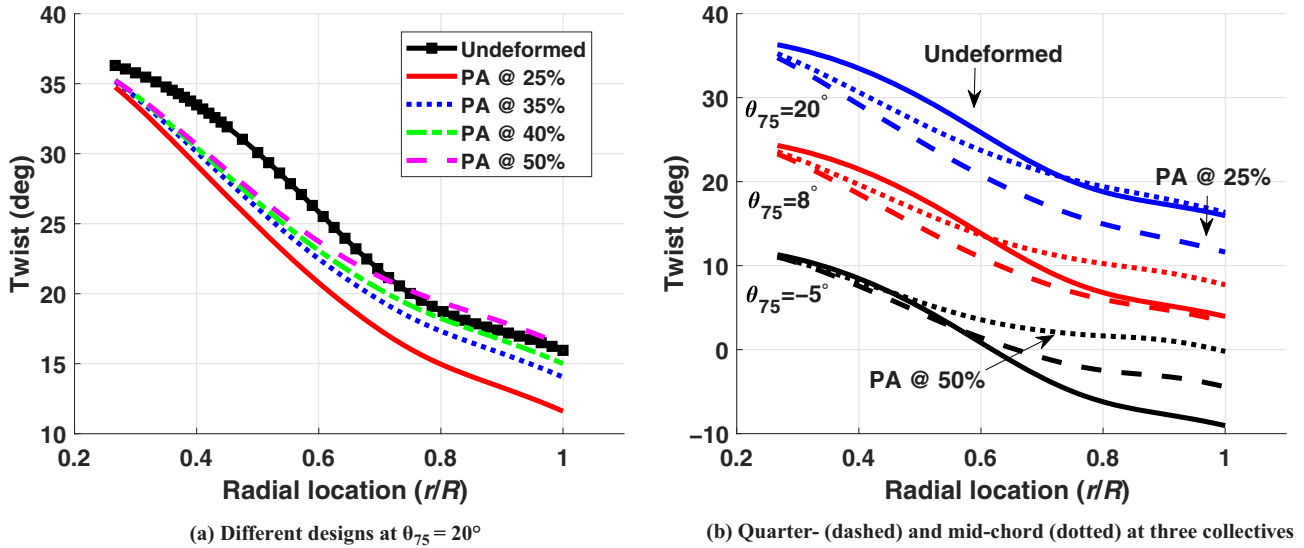


Fig. 12. Blade elastic twist in vacuum.

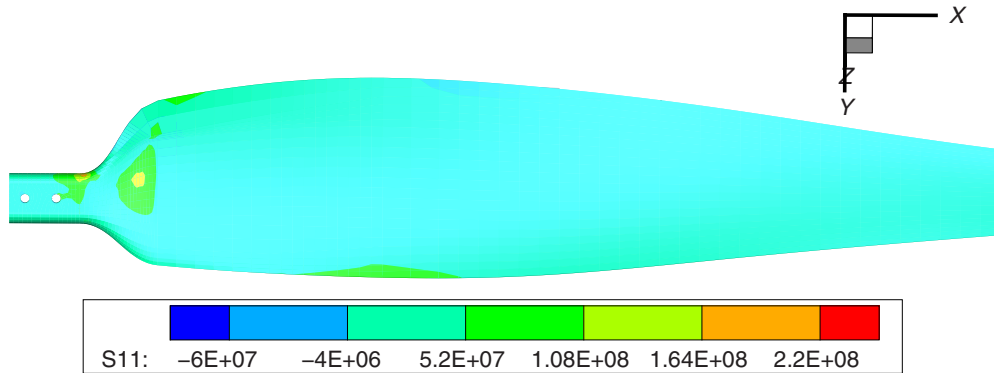


Fig. 13. Blade axial stress (σ_{11}) at the bottom surface for a collective of 20° and pitch axis of 40% chord.

torsional moment is especially important as it reduces the pitch link loads and allows for lighter servos. Previous designs required counterweights to alleviate the control loads, so moving the pitch axis will reduce the weight penalty of the counterweights or eliminate the need for them entirely.

Blade deformation

Previous work by the authors (Ref. 7) found that the elastic twist deformations are very high for ultra-thin blades, due to a combination of the high propeller moment, trapeze effect, and extremely low torsional stiffness. The trapeze effect is a phenomenon that is significant only for thin structures and will cause the blade to untwist under a tensile load. The magnitude of the deformation is related to the twist and the tensile force. In the presence of high rotational speed, the deformation caused by the trapeze effect for ultra-thin airfoils with relatively large twist is notable. The propeller moment will try to flatten the blade and is proportional to the local pitch angle. Understanding the interaction between the propeller moment and the trapeze effect for different collectives is paramount to properly designing an efficient blade.

Figure 12(a) shows the blade twist versus span for all four blade designs at a collective of 20°. There were three key conclusions that could be drawn. The first is that there was significant elastic twist occurring before the blade starts—this occurred in the transition region and was due to the high propeller moment caused by the high pitch angle. The

second is that the deformations varied considerably with pitch axis location. When the pitch axis is at 25% chord, the propeller moment was very high (shown in the previous section). This caused the blade to twist down significantly near the tip. However, when the pitch axis was moved to midchord, there was little elastic twist at the tip due to the reduced propeller moment. The last conclusion was that the elastic twist varied with radial location. For the inboard section of the midchord case, the propeller moment still caused a twist down due to the high pitch angle. However, at the outboard section the lower pitch angle reduced the propeller moment enough to where it was balanced by the trapeze effect, causing little elastic twist.

Figure 12(b) shows the blade twist versus span for three different collectives and two blade designs. For each collective, the interaction between the trapeze effect and propeller moment was different. For the lowest collective of -5°, the propeller moment was very small due to the low pitch angle. Near the tip, the local pitch angle was less than zero, so the propeller moment worked with the trapeze effect to untwist the blade, causing significant pitch deformations of almost 10° at the tip. For a moderate collective of 8°, the propeller moment and trapeze effect appear to be almost balanced for the quarter-chord design. However, since the midchord design had a significantly lower propeller moment, the trapeze effect caused it to twist up (untwist) near the tip. As mentioned previously, at a collective of 20°, the mid-chord design had little elastic twist near the tip, while the quarter-chord design had significantly higher propeller moment causing significant

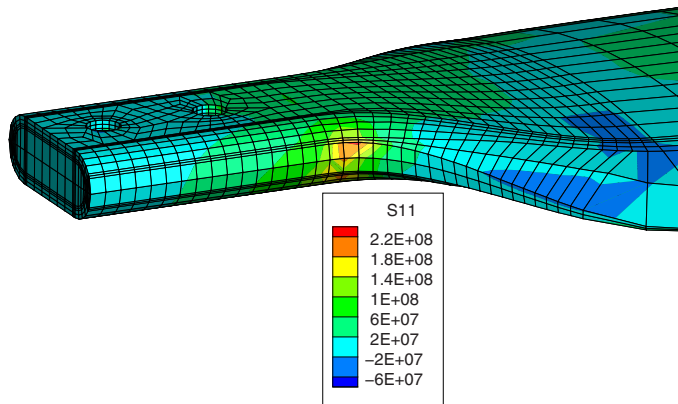


Fig. 14. Blade axial stress (σ_{11}) near the root for a collective of 20° and pitch axis of 40% chord.

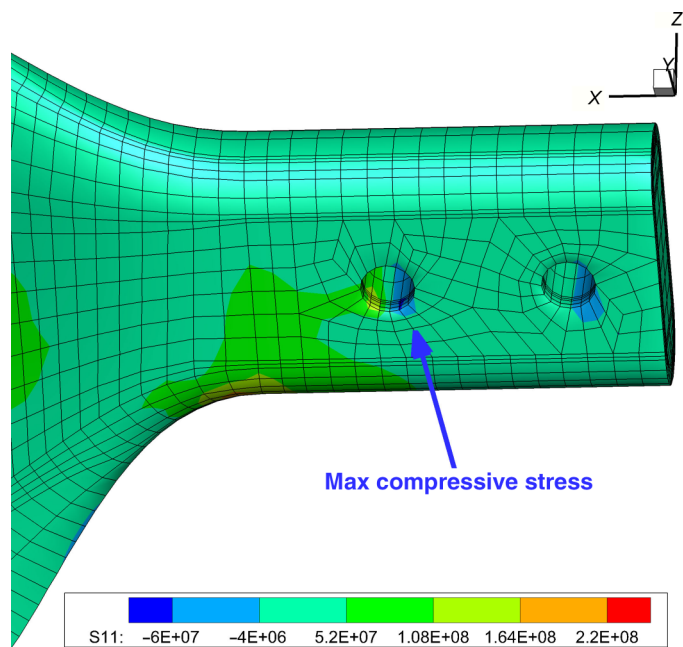


Fig. 15. Blade axial stress (σ_{11}) near the blade adapter connection for a collective of 20° and pitch axis of 40% chord.

nose down twist. Overall, moving the pitch axis backward from quarter-chord caused the blade to twist up (in reference to the quarter-chord design) from the decreased propeller moment. The significant elastic twist means that flexibility must be considered when performing aerodynamic analysis.

3D stress

Three-dimensional FEA allowed the direct examination of 3D stresses, which were used to evaluate the factor of safety of each design. The maximum tensile and compressive stresses were evaluated for the blade and blade adapter to determine the factors of safety, although only the blade results are shown here. The tensile and compressive strength of the materials are presented in Table 3.

The first step in evaluating the blade factors of safety was determining which material carried the highest stresses. Figures 13 and 14 show the blade axial stress for a collective of 20° for the design with the pitch axis at 40% chord. The bottom view of the blade shows highly localized stress

Table 5. Maximum stress versus pitch axis

Pitch Axis	Maximum Tensile Stress (MPa)	Tensile Factor of Safety	Maximum Compressive Stress (MPa)	Compressive Factor of Safety
25% chord	500	1.17	136	3.43
35% chord	307	1.91	97	4.81
40% chord	240	2.45	78	5.97
50% chord	195	3.01	52	8.93

patterns close to the root due to the high curvature of the transition region. From Fig. 14, it is clear that the maximum stress occurred at the inboard transition section near the trailing edge. One interesting observation was that the maximum stress occurred in the skin rather than the spar, likely due to the higher curvature found in the skin.

Figure 15 shows the location of the maximum compressive stress for a collective of 20° for the design with the pitch axis at 40% chord. The highest compressive stress occurred in the skin around the outboard bolt hole that attaches the blade to the blade adapter. A majority of the stress was caused by the steady axial centrifugal force but some was due to moments and shear forces caused by the C.G. offset. This resulted in the stress concentration shifting toward the trailing edge side of the bolt hole and varying with both pitch axis and collective.

Figure 16(a) shows the maximum tensile stress in the blade versus pitch angle for different blade designs. Since the maximum stresses occurred in the skin, and the skin is a 0/90 weave, both σ_{11} and σ_{22} were checked. The allowables in the 22 direction were assumed to be the same as in the 11 direction. The stresses varied considerably with both pitch axis location and collective. The trends appear to be similar to that of the torsional moment shown previously (Figs. 9(b) and 11(b)), in that moving the pitch axis to midchord and decreasing the pitch angle reduce the maximum stress.

Figure 16(b) shows the maximum compressive stress in the blade versus pitch angle for different blade designs. Similar to the maximum tensile stress, the maximum compressive stress varied with both pitch axis location and collective, with the maximum stress occurring for the quarter-chord case with high collective.

Table 5 presents the maximum tensile and compressive stresses and factors of safety for each blade design. The factors of safety for the tensile stress were much lower than the compressive stress, so the tensile stress was used to drive the design choice. To purely minimize tensile stress, the midchord pitch axis design would have been selected. However, the previous section on stability showed that the midchord design produces the lowest damping. Therefore, a pitch axis location of 40% was chosen as it provides the largest damping for a design with the factor of safety greater than 2.

Natural frequencies

Figure 17(a) shows the fan plot for the selected blade design (pitch axis at 40% chord). The four vertical lines indicate tip Mach numbers of 0.7, 0.8, 0.9, and 0.95, which are the preliminary values for testing. Figure 17(b) shows the fan plot for the baseline blade design (pitch axis at 25% chord) for reference.

The torsion coupling is apparent for the first mode, which has some torsion despite being predominately flap, as seen in Fig. 18 for the 40% blade design (quarter-chord design has similar mode shapes). The second mode, seen in Fig. 19, is pure torsion with little coupling. However, all higher modes had significant coupling. For example, the third mode for both models was a coupled lag-torsion mode and is shown in Fig. 20 for the 40% pitch axis model. This indicates that despite the reduction of the C.G. offset from moving the pitch axis to 40% chord, there was

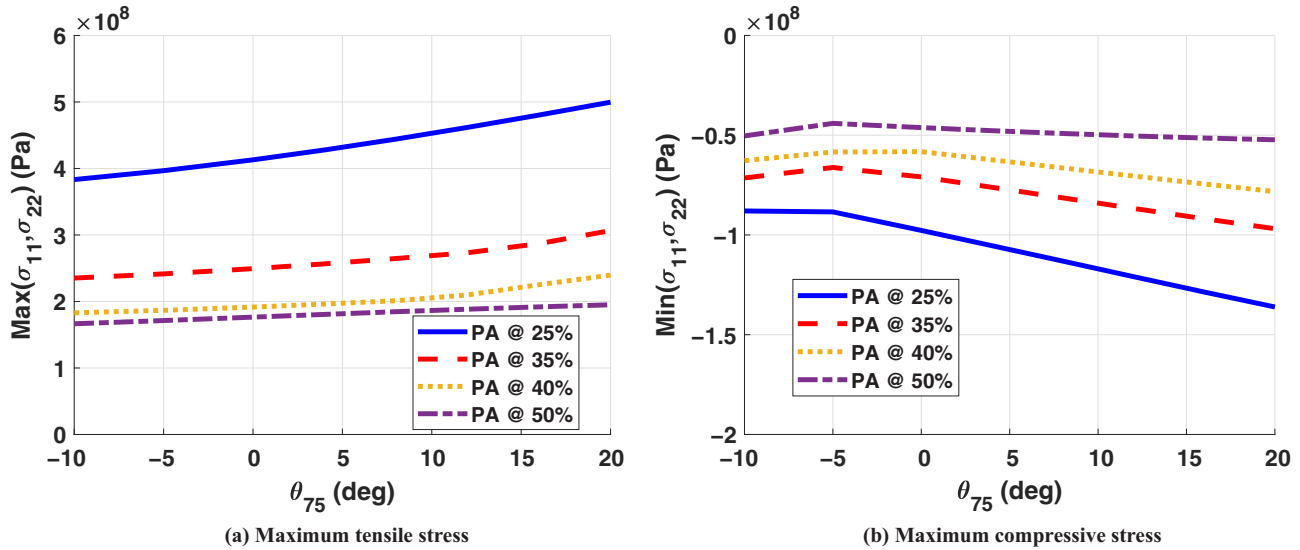


Fig. 16. Maximum stress in the blade for different collectives and blade designs.

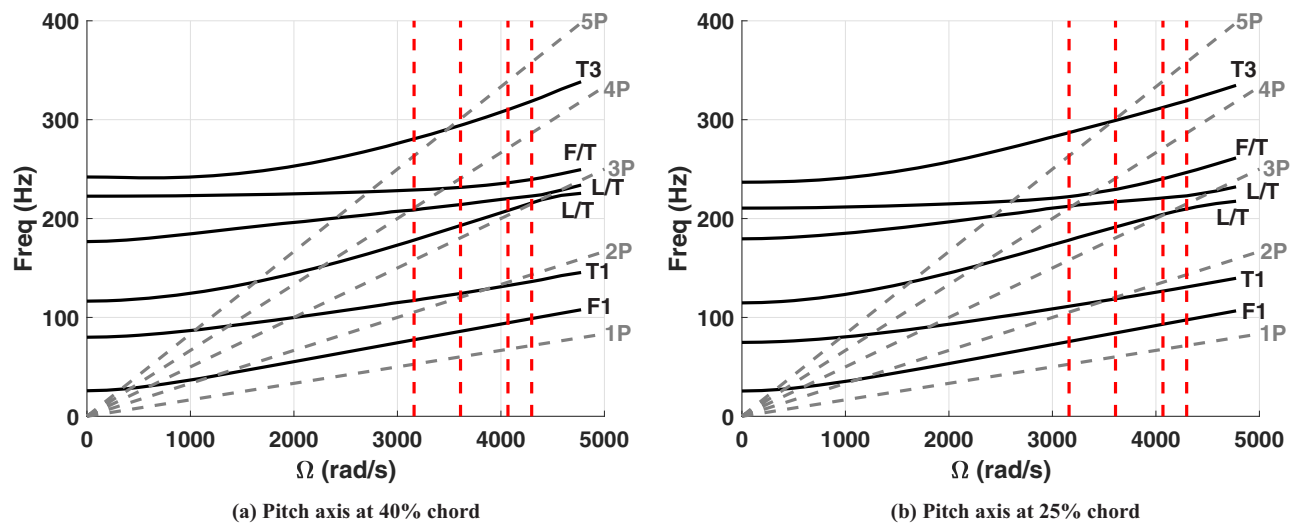


Fig. 17. Fan plot for two blade designs.

still significant torsion coupling with both flap and lag. The cause of this coupling was twofold. The C.G. offset, which remained about 10% of the chord, caused significant coupling. Additional coupling was due to the low torsional stiffness and trapeze effect, which caused high torsional deformations due to the high rotational speed. For the design with the pitch axis at 40% chord, the third mode was close to 3/rev for the highest tip Mach number case. This should be watched carefully moving forward but will likely change when the control system stiffness is finalized. These frequencies are obtained in vacuum but would not change by much if obtained in the Martian atmosphere due to the low density. The addition of an atmosphere would cause the frequencies to drop, with exact difference varying by mode. The first mode drops by just over 2%, the second mode by about 4%, and the third mode by approximately 8%.

Ideal Hover

Hover analysis was performed over a range of collective pitch angles from -10° to 20° in increments of 1° . Three tip Mach numbers were

explored, 0.7, 0.8, and 0.95, although only results for the highest Mach number are shown. In this section, the effect of aerodynamics on the blade control load is examined. Next, the effect of flexibility and sectional deformations on sectional airloads is presented. Finally, the 3D stresses are studied. As part of the hover analysis, rotor parameters such as blade loading (C_T/σ), power coefficient (C_P/σ), and figure of merit were studied. However, these values are not yet able to be released and are not published here. The atmospheric conditions used are those found at the Planetary Aeolian Laboratory (PAL) where the ROAMX blades will be tested (Ref. 9). Table 6 compares these conditions to nominal Earth values.

Blade aerodynamic model

The inflow was modeled using blade element momentum theory. Since the roll-up characteristics and core-growth are unconventional and likely unusual an elementary model was preferred in the beginning instead of free wake. Greater emphasis was placed on the unusual airfoil

Table 6. Atmospheric conditions

Parameters	Earth (Sea Level/International Standard Atmosphere)	Earth (Planetary Aeolian Laboratory)
Density (kg/m ³)	1.225	0.015
Speed of sound (m/s)	343	341
Dynamic viscosity (Ns/m ²)	1.75×10 ⁵	1.75×10 ⁵

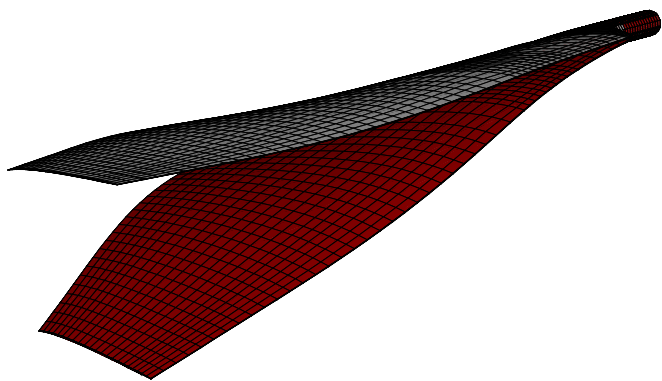


Fig. 18. First flap for the blade with the pitch axis at 40% chord and a tip Mach number of 0.95. The gray and red blades are undeformed and deformed, respectively.

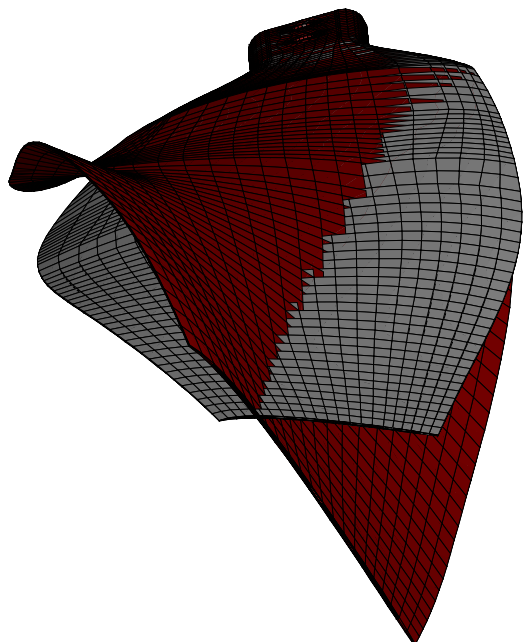


Fig. 19. First torsion for the blade with the pitch axis at 40% chord and a tip Mach number of 0.95. The gray and red blades are undeformed and deformed, respectively.

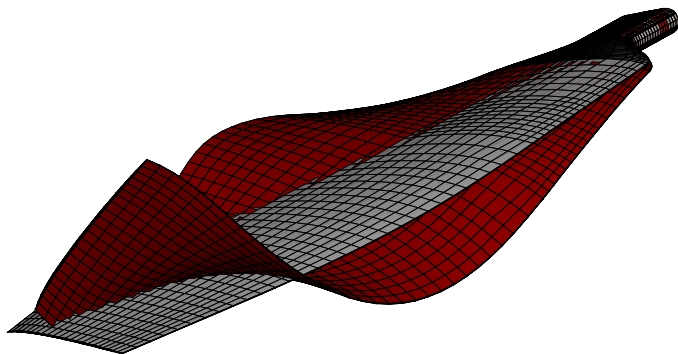


Fig. 20. Third mode (coupled torsion-lag) for the blade with the pitch axis at 40% chord and a tip Mach number of 0.95. The gray and red blades are undeformed and deformed, respectively.

decks. The blade was divided up into 18 aerodynamic segments, each with its own airfoil, Mach number (M), and Reynolds number (Re). The aerodynamic segments are shown in Fig. 21. The aerodynamics in the transition region were neglected, as the dynamic pressure was very small. For each segment, the aerodynamic forces were calculated and applied to all surface nodes within that segment. Each region had its own C81 airfoil deck provided by NASA. For each deck, the aerodynamic coefficients were functions of angle of attack and Mach number with a fixed Re/M ratio. Within each region, fine-tuning to the local Reynolds number was based on standard correction (Ref. 18).

Control load

This section studies the effect of aerodynamics on the root torsional moment (control load). The pitch control actuator must handle this load, and, therefore, it is crucial in the design process. Figure 22 presents the variation of blade torsional moment with blade loading. Most of the load was due to the inertial propeller moment, so the total moment had a similar trend as pure rotation in vacuum. Despite the location of the pitch axis behind the aerodynamic center, the net aerodynamic moment was nose-down, although the magnitude was significantly lower than the inertial moment. Therefore, the magnitude of the total control moment was only slightly higher with aerodynamics than in vacuum. The large control load will be handled by using large actuators. For when weight saving is crucial, counterweights can be used to reduce the control load to a manageable level. Though it is possible, including counterweights was not pursued in this effort.

Sectional airloads and blade deformations

This section presents the sectional spanwise airloads and blade deformations. The effect of flexibility on spanwise airloads is examined at a low ($C_T/\sigma = 0.04$) and a high ($C_T/\sigma = 0.27$) blade loading. Figure 23 shows the sectional normal force for the two cases, along with the different collectives for each case.

The effect of flexibility on the spanwise loads distribution is significant. To further understand the difference in airloads, the elastic twist is shown for both cases in Fig. 24. For the low blade loading case, significant pitch up elastic twist is seen. Despite a lower collective of 3°, the flexible blade had a higher pitch from $r/R = 0.7$ to the tip, matching the sectional airload trend shown in Fig. 23(a). For the high blade loading case, the flexible blade has a lower pitch angle at the inboard sections, despite having the same collective. However, the flexible blade had a higher pitch angle near the tip, where it outperformed the rigid blade (Fig. 23(b)).

3D stress

The 3D stresses were examined in the blade to determine the change in the factor of safety with the addition of aerodynamics. Figure 25 shows

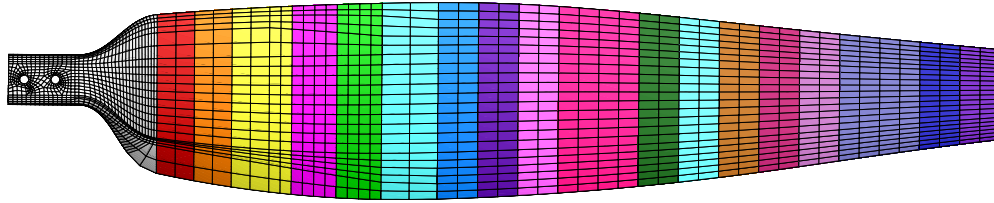


Fig. 21. The blade aerodynamic segments are shown. Aerodynamics was neglected in the transition region.

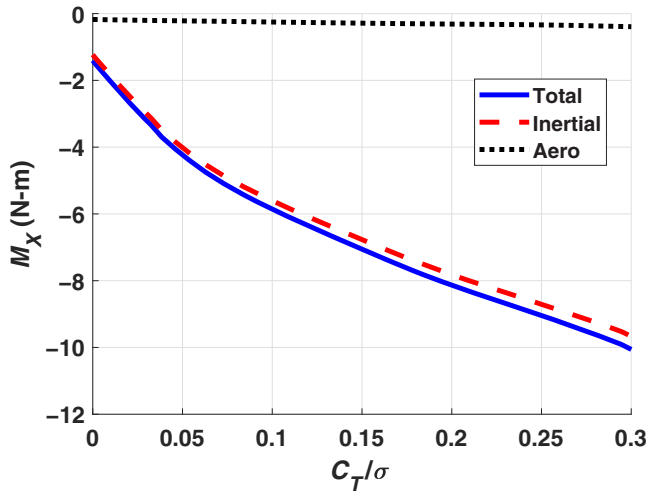


Fig. 22. Blade control load versus blade loading.

the axial stress on the blade, with Figs. 26 and 27 showing the tensile and compressive concentrations at the root. Overall, the stress patterns look identical to rotation in vacuum, and the locations of maximum stress were the same for tensile and compressive stress.

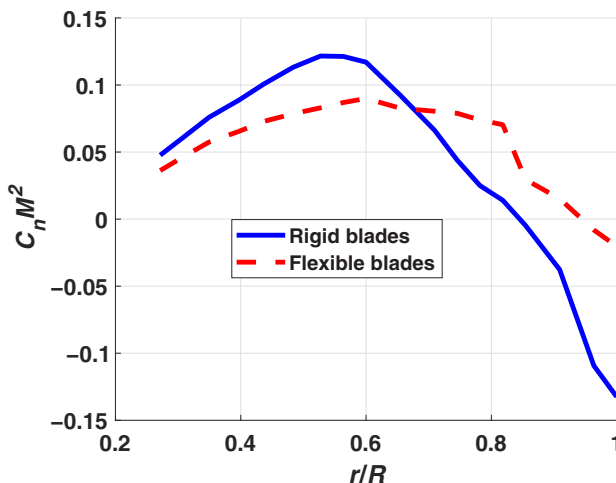
Figure 28(a) shows the maximum tensile stress in the blade versus pitch angle. For low collectives, there was no difference with and without aerodynamics. For high collectives, when the blade loading was at its maximum, there was a small increase in maximum tensile stress of about 5%. Figure 28(b) shows the maximum compressive stress in the blade

versus collective. Similar to the maximum tensile stress, the addition of aerodynamics only makes a difference for high collectives. The increase in maximum compressive stress was about 4% with aerodynamics for a collective of 20°. The almost negligible effect of aerodynamics on the blade stresses was due to the extremely low density and high rotational speed. The maximum thrust produced by one blade was less than 1% of the centrifugal force, so the loads and stresses were dominated by the inertial terms.

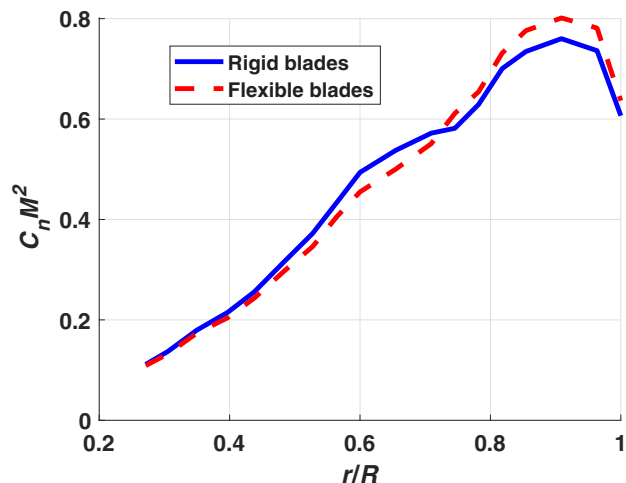
Tables 7 and 8 present the maximum tensile and compressive stresses in the blade with and without aerodynamics for several blade collectives. The final factor of safety with aerodynamics is also shown. Similar to pure rotation in vacuum, the factor of safety was much higher for compressive stress than for tensile stress. In steady hover with a collective of 20°, the factors of safety for tensile and compressive stress were 2.33 and 5.73, respectively.

Hover with Cyclic

This section studies the dynamic loads in hover with cyclic applied. During testing, there will be perturbations and oscillations, caused by recirculation, small differences between the blades, or changes in the rotational speed. The low Lock number will cause these oscillations to damp out very slowly and persist for a number of revolutions. Therefore, the maximum loads produced by these oscillations must be taken into account during the design process. The oscillatory control load and dynamic 3D stress are needed to design the control actuators and blade. Although the vibrations can occur at varying frequencies, 1/rev will be the dominant forcing, so varying lateral cyclics were applied to simulate the perturbations. Similar to the previous sections, all

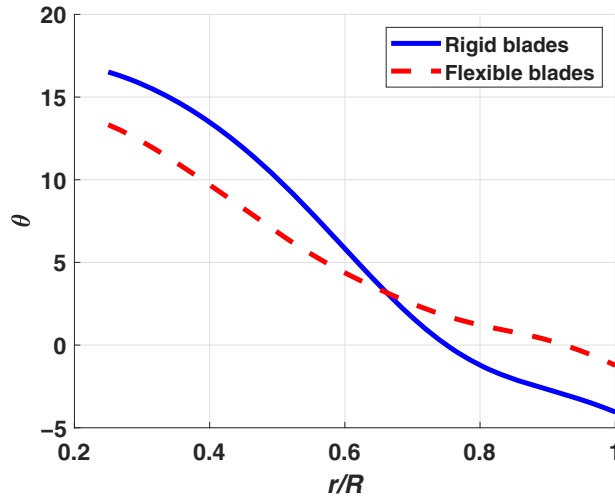


(a) $C_T/\sigma = 0.04$. $\theta_{75} = 0^\circ$ for the rigid and -3° for the flexible blades

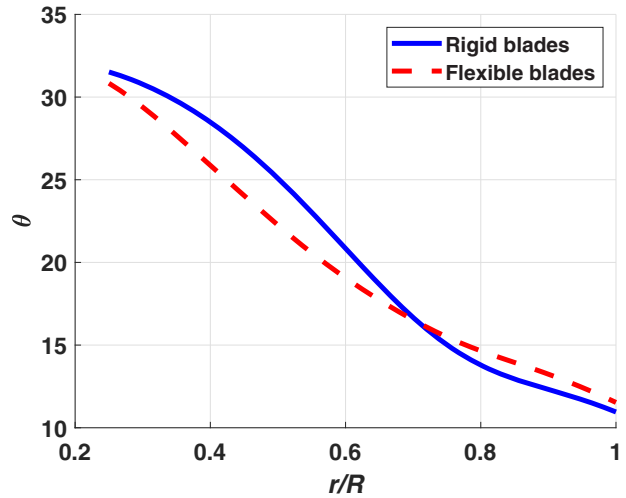


(b) $C_T/\sigma = 0.27$. $\theta_{75} = 15^\circ$ for both the rigid and flexible blades

Fig. 23. Hover sectional normal force.



(a) $C_T/\sigma = 0.04$, $\theta_{75} = 0^\circ$ for the rigid and -3° for the flexible blades



(b) $C_T/\sigma = 0.27$, $\theta_{75} = 15^\circ$ for both the rigid and flexible blades

Fig. 24. Hover sectional twist.

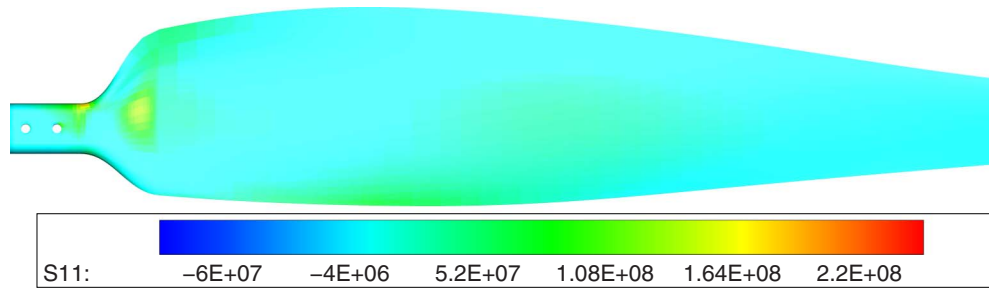


Fig. 25. Blade axial stress (σ_{11}) in hover at the bottom surface for a collective of 20° .

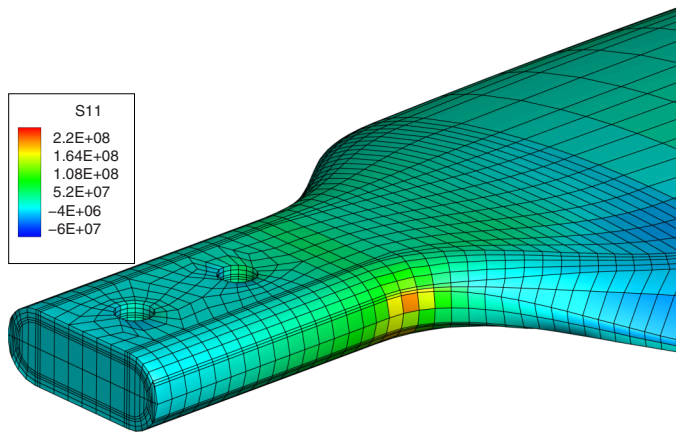


Fig. 26. Blade axial stress (σ_{11}) in hover at the root for a collective of 20° .

results presented were obtained for the highest tip Mach number of 0.95.

Oscillatory control load

The oscillatory control load is presented in Fig. 29 for a collective of 20° and lateral cyclics of 1° , 2° , and 5° . As expected, the behavior for all cases was strongly 1/rev due to the cyclic. However, the peaks were shifted by about 90° from what was expected. Based on the static

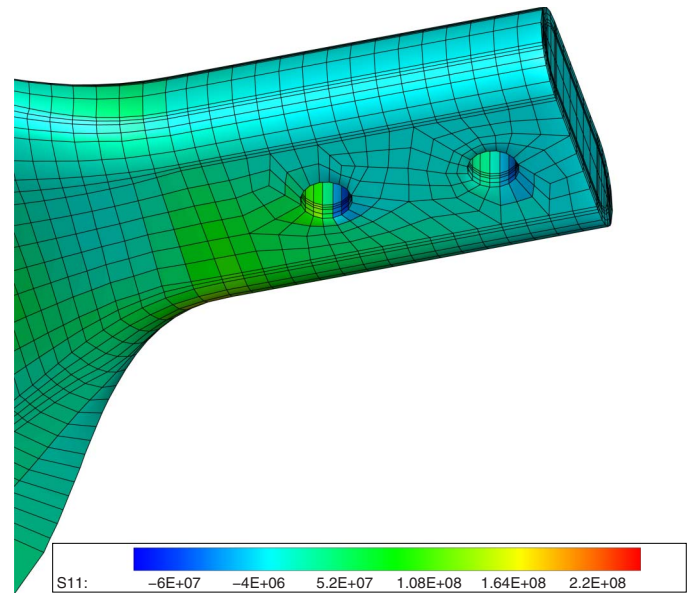


Fig. 27. Blade axial stress (σ_{11}) in hover near the blade adapter connection for a collective of 20° .

propeller moment, the magnitude of M_X should have been at a maximum at 0° , when the pitch angle was highest. The fact that there was a phase shift indicates that the inertial terms dominated the oscillatory behavior,

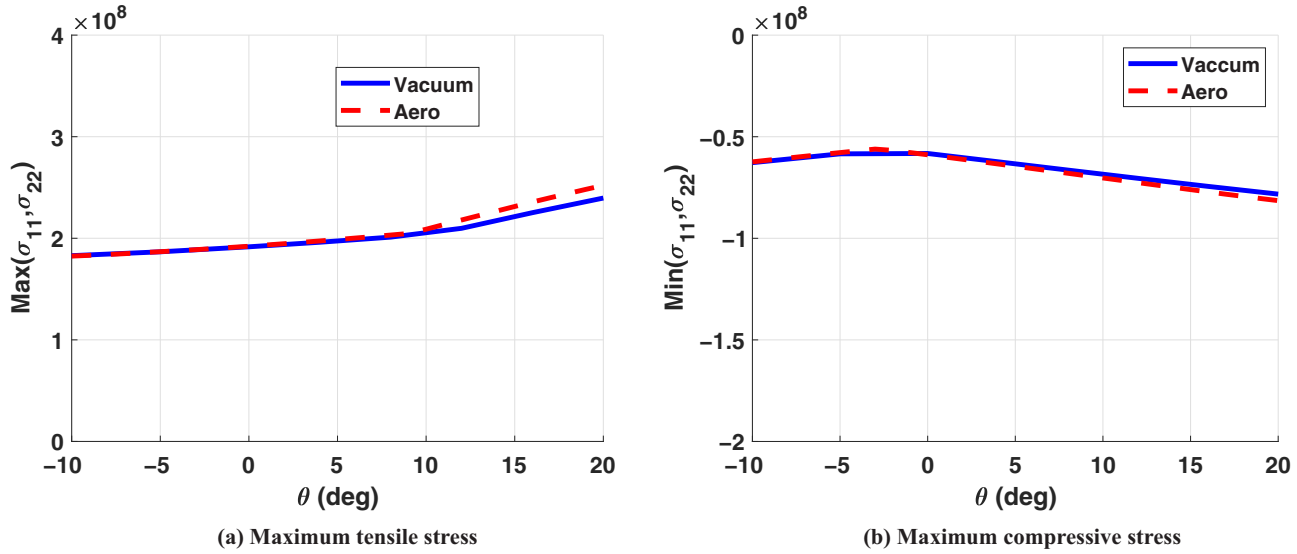


Fig. 28. Effect of aerodynamics on maximum stress.

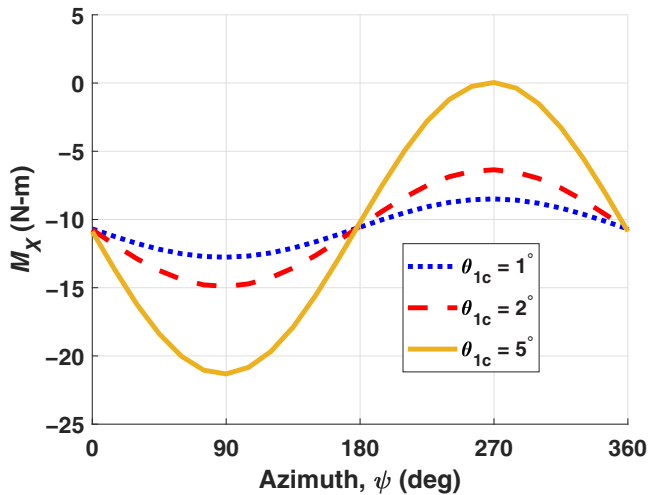


Fig. 29. Oscillatory control load for a collective of 20° and lateral cyclics of 1°, 2°, and 5°.

Table 7. Maximum tensile stress with aerodynamics

θ_{75}	Vacuum σ_{11} (MPa)	Aero σ_{11} (MPa)	Aero Factor of Safety
-10°	183	182	3.22
-5°	187	187	3.13
4°	196	197	2.97
12°	209	218	2.69
20°	240	252	2.33

due to the C.G. offset and high rotational speed. The influence of aerodynamic moment was assumed to be minimal based on Fig. 22 from the previous section. Another indication that inertial terms dominated was that the control load peak-to-peak was much higher than the change in torsional moment seen for steady hover (Fig. 22 covered approximately 25° and varied by less than 10 N-m, while Fig. 29 covered only 10° and has a peak-to-peak of over 20 N-m).

Figure 30(a) presents the torsional moment peak-to-peak versus collective for the different cyclic values. The amplitude was steady with

Table 8. Maximum compressive stress with aerodynamics

θ_{75}	Vacuum σ_{11} (MPa)	Aero σ_{11} (MPa)	Aero Factor of Safety
-10°	63	63	7.41
-5°	58	58	8.05
4°	62	63	7.41
12°	70	73	6.40
20°	78	81	5.77

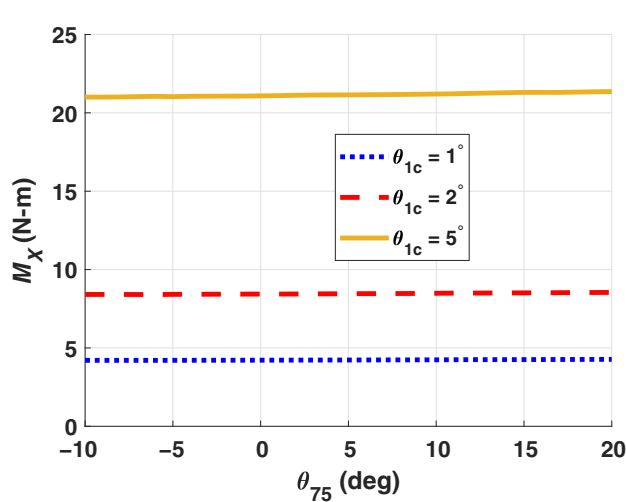
collective and varied linearly with cyclic. Figure 30(b) shows the maximum control load versus collective for different lateral cyclics. Overall, the inertial forcing increased the loads significantly, although the propeller moment still made up a substantial portion of control load. The actuator and pitch links must be sized to handle not just the high steady loads but also the oscillatory loads that will be made more important by the low aerodynamic damping.

Dynamic 3D stress

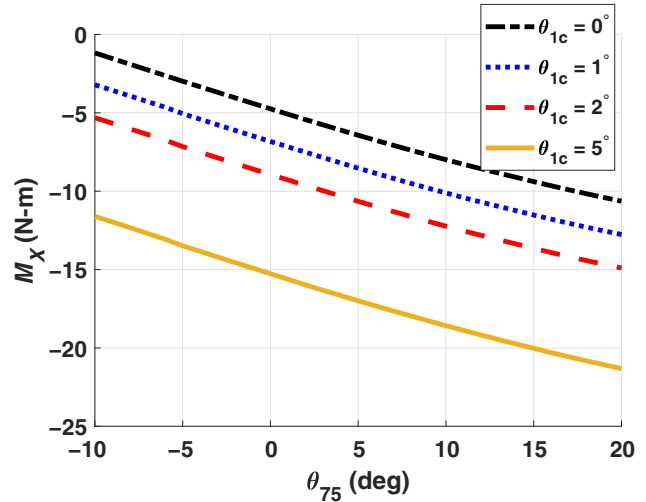
Figures 31(a) and 31(b) show the maximum tensile and compressive stress for the blade versus azimuth for a collective of 20° and different lateral cyclics. In general, the behavior is 1/rev, except for the tensile stress between 150° and 240° for the 5° cyclic case. Recall that the maximum of σ_{11} and σ_{22} is used; typically σ_{11} is higher; however, for the 5° cyclic case between 150° and 240°, σ_{22} is greater than σ_{11} , causing the break in 1/rev behavior. Overall, the maximum tensile and compressive stress occur at 45°, offset from the maximum control moment by 45°.

Figure 32 shows the individual variation of σ_{11} and σ_{22} over one revolution for a lateral cyclic of 2° and 5°. It is evident that the mean value for σ_{22} is lower than σ_{11} , but a phase offset causes σ_{22} to become the critical stress for approximately 90°. Another interesting observation from Fig. 32 is that σ_{22} for a lateral cyclic of 5° is not 1/rev. This is due to the location of maximum stress varying during a revolution—the stress at any single point is 1/rev.

Figure 33 shows the axial stress (σ_{11}) at the blade root for an azimuth of 45° and 225° with the highest lateral cyclic ($\theta_{1c} = 5^\circ$). The maximum stresses occurred at the same location as seen previously; however, the magnitude and the localized stress pattern changed with azimuth. Figure 34 shows the maximum tensile and compressive stresses present

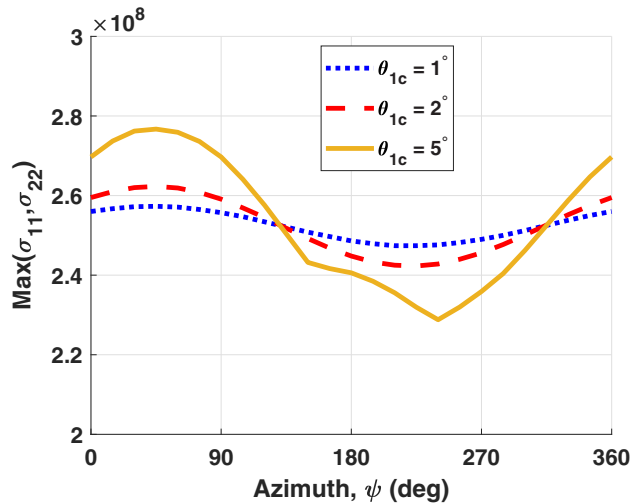


(a) Control load peak to peak

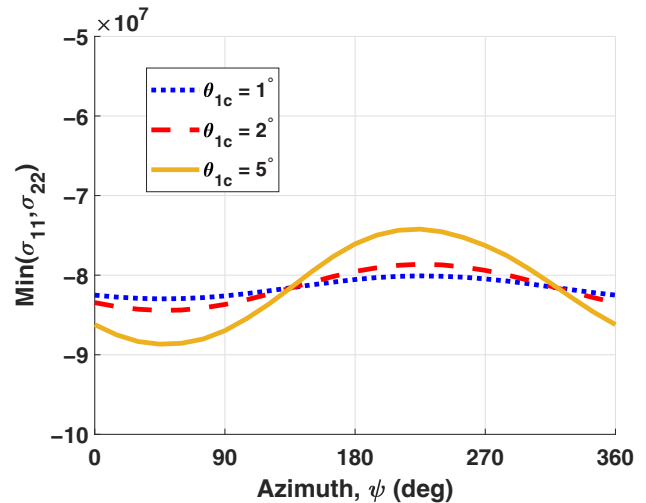


(b) Maximum control load

Fig. 30. Oscillatory control load characteristics versus collective for lateral cyclics of 1°, 2°, and 5°.



(a) Maximum tensile stress



(b) Maximum compressive stress

Fig. 31. Maximum blade stress versus azimuth for a collective of 20° lateral cyclics of 1°, 2°, and 5°.

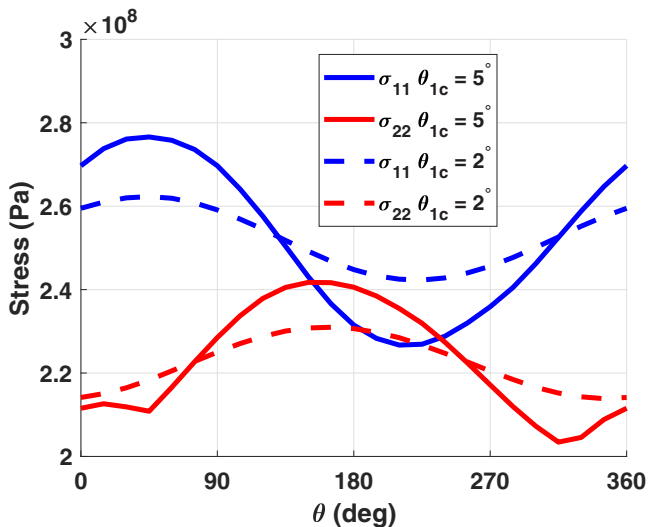


Fig. 32. Maximum blade tensile stress for a collective of 20° and lateral cyclics of 2° and 5°.

in the blade versus collective for various lateral cyclics. The addition of cyclics increased the maximum stresses through inertial forcing, but the steady centrifugal force still remained the dominant load. Both the maximum tensile and compressive stresses increased by approximately 10% to 278 and 89 MPa, respectively (for $\theta_{75} = 20^\circ$ and $\theta_{1c} = 5^\circ$). This brought the final factors of safety to 2.12 and 5.27, still well within the material limits.

Conclusions

An aeromechanical analysis of rotor blades with unusually thin, unconventional airfoils was conducted in support of the NASA ROAMX project. The main objective was to design the internal structure of the rotor blade and blade adapter to achieve sufficient factors of safety for hover testing. In support of this objective, the aeroelastic behavior of these unique designs was studied. Stability analysis, structural analysis in vacuum, and comprehensive analysis in both steady and unsteady hover were performed. Four different blade designs were considered, each with a different C.G. offset obtained by shifting the pitch axis

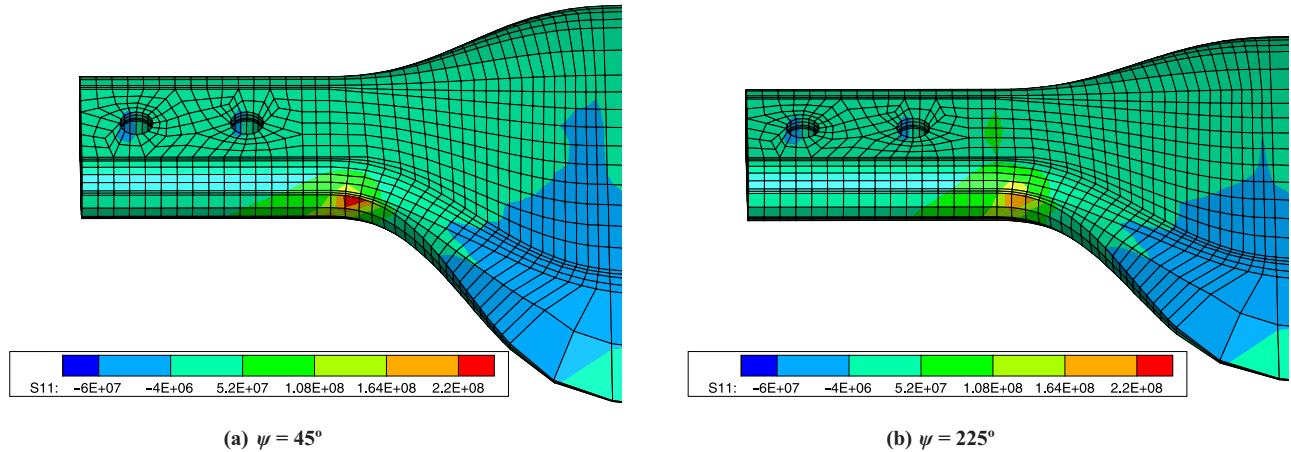


Fig. 33. Axial bending stress (σ_{11}) for $\theta_{75} = 20^\circ$ and $\theta_{1c} = 5^\circ$.

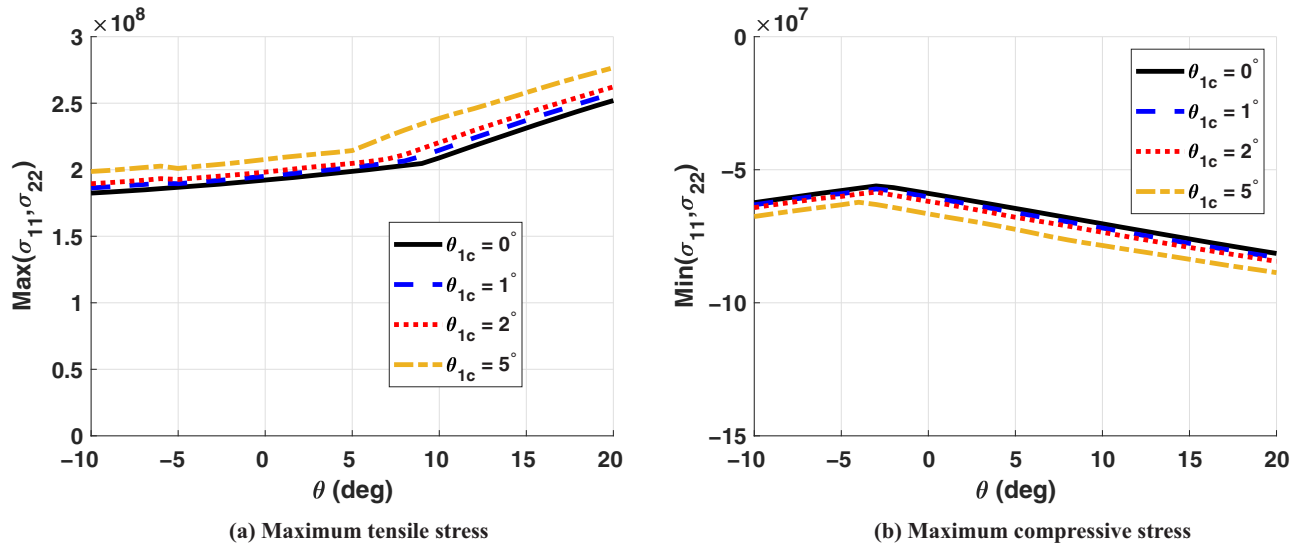


Fig. 34. Maximum tensile and compressive stress versus collective for different lateral cyclics.

before one was chosen for aerodynamic analysis. Blade damping, natural frequencies, blade deformations, root loads, and 3D stresses were all studied. This work yields the following conclusions:

- 1) The selected blade design with the pitch axis at 40% chord is safe and stable for all preliminary test conditions, with a factor of safety greater than two and over 1% torsional damping.
- 2) Minimizing the C.G. offset, achieved by moving the pitch axis close to midchord was crucial in reducing the blade root loads and 3D stresses. The propeller moment was reduced by 30%-40%, the blade in-plane lag force and flapping moment reduced by two and one order of magnitude respectively, and the blade stresses reduced by over 50%.
- 3) Significant elastic pitch deformation was observed for all blade designs, with the exact behavior varying with collective. This phenomenon was due to the interaction of the trapeze effect and propeller moment and must be included when modeling ultra-thin blades.
- 4) The blade control loads were significantly increased by the addition of oscillations through lateral cyclic perturbations. This increase was primarily inertial in nature and due to the pitch-flap coupling from the C.G. offset. The high peak-to-peak values imply fatigue must be considered when designing the pitch links.

The unusual nature of the blades and unique atmosphere means confidence in design and analysis will not mature without systematic valida-

tion. Validation for these unique blades should go beyond usual performance and is recommended in the form of blade strains at a minimum and deformations and roll-up in the future. Two sets of blades, with the pitch axis at 40% and 25% chord, would be interesting test cases. In conclusion, testing for Mars conditions is likely to reveal new and interesting opportunities to optimize rotor blades that are unavailable on Earth—unless at very high altitudes—but crucial and enabling for larger more capable helicopters on Mars.

Acknowledgments

This work is supported partially by the NASA NIA Award No. 202060 with Haley Cummings as the Technical Point of Contact and Susan Gorton as the Sponsor. The support of the Aeromechanics Branch at NASA Ames Research Center is gratefully acknowledged.

References

- ¹Savu, G. and Trifu, O., "Photovoltaic Rotorcraft for Mars Missions," Proceedings of the 31st AIAA/ASME/SAE/ASEE Joint Propulsion Conference and Exhibit, San Diego, CA, July 10–12, 1995, pp. 1995–2644.

²Young, L., and Edwin, W. A., “Vertical Lift Planetary Aerial Vehicles: Three Planetary Bodies and Four Conceptual Design Cases,” Proceedings of the 27th European Rotorcraft Forum, Moscow, Russia, September 11–14, 2001.

³Datta, A., Roget, B., Griffiths, D., Pugliese, G., Sitaraman, J., Bao, J., Liu, L., and Gamard, O., “Design of a Martian Autonomous Rotary-Wing Vehicle,” *Journal of Aircraft*, Vol. 40, (3), May 2003, pp. 461–472, DOI: 10.2514/2.3141.

⁴Balaram, J., Daubar, I. J., Bapst, J., and Tzanetos, T., “Helicopters on Mars: Compelling Science of Extreme Terrains Enabled by an Aerial Platform,” Paper 2089, Proceedings of the Ninth International Conference on Mars, Pasadena, CA, July 22–25, 2019.

⁵Pipenberg, T. B., Keennon, T. W., Langberg, A. S., and Tyler, D. J., “Development of the Mars Helicopter Rotor System,” Proceedings of the 75th Annual Forum of the American Helicopter Society, Philadelphia, PA, May 13–16, 2019.

⁶Johnson, W., Withrow, S., Young, L., Malpica, C., Koning, W. J. F., Kuang, W., Fehler, M., Tuano, A., Chan, A., Datta, A., Chi, C., Lumba, R., Escobar, D., Bob Balaram, J., Tzanetos, T., and Grip, H. F., “Mars Science Helicopter Conceptual Design,” NASA TM 2020 220485, 2020.

⁷Chi, C., Lumba, R., Jung, Y. S., and Datta, A., “Aeromechanical Analysis of a Next-Generation Mars Hexacopter Rotor,” *Journal of Aircraft*, Vol. 59, (6), November 2022, pp. 1463–1477, DOI: 10.2514/2.3141.

⁸Koning, W. J. F., Romander, E. A., and Johnson, W., “Optimization of Low Reynolds Number Airfoils for Martian Rotor Applications Using an Evolutionary Algorithm,” Proceedings of the AIAA Scitech 2020 Forum, AIAA, Orlando, FL, January 6–10, 2020.

⁹Cummings, H., Perez Perez, N., Koning, W., Johnson, W., Young, L., Haddad, F., Romander, E., Balaram, J., Tzanetos, T., Bowman, J., Wagner, L., Withrow-Maser, S., Isaacs, E., Toney, S., Shirazi, D., Conley, S., Pipenberg, B., Datta, A., Lumba, R., Chi, C., Smith, K., Cornelison, C., Perez, A., Nonomura, T., and Asai, K., “Overview and Introduction of the Rotor Optimization for the Advancement of Mars eXploration

(ROAMX) Project,” Proceedings of the Vertical Flight Society Aeromechanics for Advanced Vertical Flight Technical Meeting, San Jose, CA, January 25–27, 2022.

¹⁰Okamoto, M., Yasuda, K., and Azuma, A., “Aerodynamic Characteristics of the Wings and Body of a Dragonfly,” *Journal of Experimental Biology*, Vol. 199, (2), February 1996, pp. 281–294, DOI: 10.1242/jeb.199.2.281.

¹¹Winslow, J., Otsuka, H., Govindarajan, B., and Chopra, I., “Basic Understanding of Airfoil Characteristics at Low Reynolds Numbers (10^4 – 10^5),” *Journal of Aircraft*, Vol. 55, (3), May 2018, pp. 1050–1061, DOI: 10.2514/1.C034415.

¹²Escobar, D., Chopra, I., and Datta, A., “High-Fidelity Aeromechanical Analysis of Coaxial Mars Helicopter,” *Journal of Aircraft*, Vol. 58, (3), May 2021, pp. 609–623, DOI: 10.2514/1.C035895.

¹³Datta, A., “X3D-A 3D Solid Finite Element Multibody Dynamic Analysis for Rotorcraft,” Proceedings of the American Helicopter Society Technical Meeting on Aeromechanics Design for Vertical Lift, San Francisco, CA, January 20–22, 2016, pp. 20–22.

¹⁴Staruk, W., and Datta, A., “Gimbale Tiltrotor Conversion Flight Loads Prediction Using Three-Dimensional Structural Analysis,” *Journal of Aircraft*, Vol. 56, (2), March 2019, pp. 758–770, DOI: 10.2514/1.C035075.

¹⁵Patil, M., and Datta, A., “A Scalable Time-Parallel Solution of Periodic Rotor Dynamics in X3D,” *Journal of the American Helicopter Society*, **66**, 042007 (2021), DOI: 10.4050/JAHS.66.042007.

¹⁶Chi, C., Datta, A., Chopra, I., and Chen, R., “Three-Dimensional Strains on Twisted and Swept Composite Rotor Blades in Vacuum,” *Journal of Aircraft*, Vol. 58, (1), January 2021, pp. 1–16, DOI: 10.2514/1.C035746.

¹⁷Sutherland, J., and Datta, A., “Fabrication, Testing, and 3D Comprehensive Analysis of Swept-Tip Tiltrotor Blades,” *Journal of American Helicopter Society*, **68**, 012002 (2023), DOI: 10.4050/JAHS.68.012002.

¹⁸Yamauchi, G., and Johnson, W., “Trends of Reynolds Number Effects on Two-Dimensional Airfoil Characteristics for Helicopter Rotor Analyses,” NASA TM 84363, 1983.